Chemical Science

ROYAL SOCIETY OF CHEMISTRY

EDGE ARTICLE

View Article Online
View Journal

Cite this: DOI: 10.1039/d6sc02363k

All publication charges for this article have been paid for by the Royal Society of Chemistry

Atomic modulation of Na^+ transport channels to enhance rate and cycling performance of tunnel-type sodium manganese oxides

Chen Xu,[a] Qinghua Yi,[a] Kaibin Feng,[a] Jie Lai,[a] Zhihao Lin,[a] Yuanhao Zheng,[b] Xiao Yan,[b] Xi Chen,[c] Chenchen Wang*[a] and Zhe Hu *[a]

Tunnel-structured $Na_{0.44}MnO_2$ is considered a promising cathode material for large-scale sodium-ion batteries due to its low cost, excellent air stability, and compatibility with sodium compensation strategies; however, its practical application is hindered by sluggish Na^+ diffusion kinetics and poor cycling stability arising from intrinsically constrained ion migration pathways and increased structural disorder during cycling. In this work, a tunnel-type $Na_{0.44}Mn_{0.89}Cu_{0.01}Ti_{0.1}O_2$ cathode is rationally designed *via* atomic modulation, which effectively widens Na^+ diffusion channels and constructs preferential transport pathways, thereby reducing the Na^+ migration energy barrier and improving the rate performance. Meanwhile, the ordering of Mn–O bonds is improved during charge–discharge processes, leading to enhanced structural stability and prolonged cycling life. As a result, the material delivers a high capacity retention of 90.4% after 1000 cycles at a high current density of 600 mA g^{-1}, demonstrating that the dual-substitution strategy is an effective approach for developing high-rate and long-lifespan cathode materials for rechargeable sodium-ion batteries.

Received 23rd March 2026
Accepted 14th May 2026

DOI: 10.1039/d6sc02363k

rsc.li/chemical-science

Introduction

Sodium-ion batteries (SIBs) have emerged as a promising complementary technology to lithium-ion batteries (LIBs) for large-scale energy storage applications.[1–3] owing to the abundant availability of sodium resources and their relatively low cost. Efforts to develop high-performance SIBs have increasingly focused on advanced cathode materials,[4–6] and the recent discovery of lithium and sodium replenishment technologies has enabled the practical utilization of cathode materials with severely insufficient sodium content under stoichiometric conditions.[7–10] Among these candidates, the tunnel-type oxide $Na_{0.44}MnO_2$ (NMO) features a unique crystal structure with multiple S-shaped sodium-ion transport pathways, intrinsic moisture resistance, and excellent structural stability, making it a highly promising cathode material for sodium-ion batteries,[11–15] The S-shaped tunnels, however, impose considerable interionic interactions during Na^+ migration, which limits the reaction kinetics. In addition, NMO suffers from low electronic conductivity and Mn^{3+}-induced Jahn–Teller distortion, constraining its rate capability and cycling stability.[16–20]

Elemental doping has been widely explored as an effective strategy to tailor the electrochemical properties of NMO. Ti doping introduces a charge compensation mechanism that stabilizes the crystal structure by regulating the Mn^{3+}/Mn^{4+} ratio.[21–27] Other dopants, including Li,[28,29] Mg,[30] Fe,[31] B,[32] and Ca[33], have been reported to enhance tunnel-type oxides through metal–oxygen bond strengthening, suppression of Jahn–Teller distortion, and activation of additional redox couples. Despite these structural and electrochemical improvements, most modified NMO materials still suffer from limited rate capability and insufficient long-term cycling stability, which highlights the necessity of rational multi-element doping strategies to achieve synergistic optimization and overcome the intrinsic limitations of NMO.

Herein, we demonstrate a Cu/Ti co-doping strategy to address the bottlenecks in Na^+ ion transport and structural stability of NMO. Combined experimental data and density functional theory (DFT) calculations reveal that the co-doping strategy enhances the ordering of Mn–O bonds during electrochemical reactions, suppresses crystal structure change during cycling, and thereby improves cycling stability. In addition, the Cu–O bond length is longer than that of the original Mn–O bond, which enlarges the Na^+ transport channels and consequently optimizes Na^+ transport kinetics. The as-prepared $Na_{0.44}Mn_{0.89}Cu_{0.01}Ti_{0.1}O_2$ cathode delivers improved rate performance, achieving a specific capacity of 104 mA h g^{-1} at

[a]Guangdong Provincial Key Laboratory of New Energy Materials Service Safety, College of Materials Science and Engineering, Shenzhen University, Shenzhen, Guangdong 518055, China. E-mail: wangcc@szu.edu.cn; huzhe@szu.edu.cn

[b]Institute of Technology for Future Industry, Shenzhen University of Information Technology, Shenzhen, Guangdong 518172, China

[c]Department of Physics, School of Mathematics and Physics, Xi'an Jiaotong-Liverpool University, 111 Ren'ai Road, Suzhou Industrial Park, Suzhou 215123, P.R. China

0.2C and retaining 81.7% of this capacity (85 mA h g^{-1}) at a high rate of 5C. Moreover, it exhibits excellent cycling stability, with a capacity retention of 90.4% after 1000 cycles at 5C.

Results and discussion

NMO and Ti-doped $Na_{0.44}Mn_{1-x}Ti_xO_2$ materials (x = 0.05, 0.1 and 0.15, labeled as NMO-T5, 10, and 15, respectively) were synthesized *via* a solid-state reaction. The XRD patterns demonstrate that all diffraction peaks correspond to the orthorhombic tunnel structure with the space group of *Pbam* (Fig. 1a and S1). NMO-T10 exhibits the most optimal electrochemical performance, while further increasing the Ti content leads to a noticeable deterioration in rate performance (Fig. S2).[34] Next, Cu/Ti co-doped materials were synthesized through a solid-state reaction. According to the Cu/Ti ratio, the as-prepared Cu/Ti co-doped NMO were labeled as $Na_{0.44}Mn_{0.895}Cu_{0.005}Ti_{0.1}O_2$ (NMO-C0.5T10), $Na_{0.44}Mn_{0.89}Cu_{0.01}Ti_{0.1}O_2$ (NMO-C1T10), $Na_{0.44}Mn_{0.88}Cu_{0.02}Ti_{0.1}O_2$ (NMO-C2T10) and $Na_{0.44}Mn_{0.87}Cu_{0.03}Ti_{0.1}O_2$ (NMO-C3T10). The XRD profiles of Cu/Ti co-doped NMO materials are summarized in Fig. 1a and S3. The results show that all the prepared samples can be indexed to pure tunnel structures with the space group of *Pbam*. The Rietveld refinements of the as-prepared materials are displayed in Fig. 1b and S4, and crystallographic parameters are shown in Tables S1 and S2. The refined unit cell parameters are shown in Fig. 1c. The lattice parameters a and c of NMO-C1Ti10 expand by 0.47% and 0.55% relative to pristine NMO, respectively. (Table S2). Moreover, the refined data indicate that Ti^{4+} ions occupy the Mn3 site, which is consistent with previous reports,[21] while Cu^{2+} ions are located at the square-pyramidal Mn5 site (Fig. S5). The as-prepared materials show improved rate performance (Fig. S6). In particular, NMO-C1T10 shows the best rate performance. Further investigations are focused on NMO-C1T10 to clarify the relationships between the improved electrochemical performance and its unique structure.

The high-resolution transmission electron microscopy (HRTEM) and selected-area electron diffraction (SAED) analysis of the optimal NMO-C1T10 sample confirmed its high crystallinity (Fig. 1d and e). The measured interplanar spacings (0.2925 nm for (001) and 0.4707 nm for (200)) were slightly larger than those of pristine NMO, directly corroborating the doping-induced lattice expansion. Transmission electron microscopy-energy dispersive spectroscopy (TEM-EDS) mapping confirmed the homogeneous distribution of Na, Mn, Cu, Ti, and O elements (Fig. 1f). The atomic compositions of the as-prepared NMO-C1T10 sample are confirmed by inductively coupled plasma optical emission spectroscopy (ICP-OES) analysis, as shown in Table S3, which demonstrates that the target stoichiometry is achieved. The morphologies of the NMO and Cu/Ti doped samples are further characterized by scanning electron microscopy (SEM). It was revealed that all the samples exhibit a rod-like morphology with particle size ranging from 1–5 μm (Fig. S7).

Fig. 2a and b show the initial five charge/discharge curves of NMO and NMO-C1T10 cathodes at 0.2C (1C = 120 mA g^{-1}). The NMO cathode exhibits six distinct voltage plateaus (Fig. 2a), corresponding to multi-stage phase transitions and Na^+/vacancy ordering during sodium insertion/extraction.[35,36] In contrast, NMO-C1T10 showed smooth charge–discharge profiles with a long slope curve between 2.4 and 3.25 V (Fig. 2b), indicating a shift from a multi-phase to a solid–solution reaction mechanism.[37] In particular, the charge–discharge curves of NMO-C1T10 exhibit excellent overlap from the 1st to the 5th cycle, demonstrating its favorable electrochemical reversibility. Besides, the broader redox peaks observed in CV (Fig. S8) suggest a more gradual and distributed ion insertion/extraction process. This mitigates localized strain and stress fluctuations during cycling, which is ultimately more favorable for long-term structural stability. Although the initial discharge capacity of

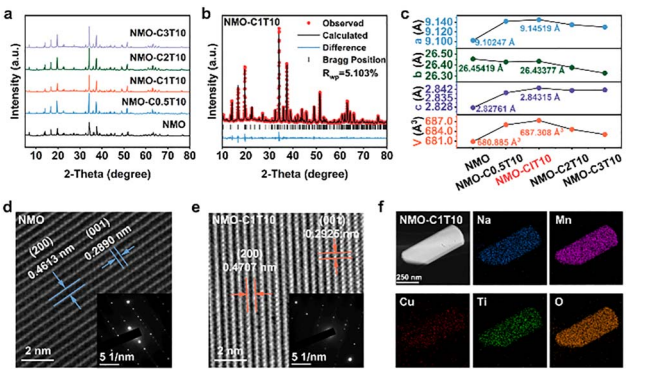

Fig. 1 (a) XRD patterns of NMO and Cu/Ti co-doped NMO. (b) Rietveld refinement results of NMO-C1T10. (c) Unit cell parameters of NMO and Cu/Ti co-doped NMO. HRTEM images (insets show the corresponding TED patterns) of (d) NMO and (e) NMO-C1T10 samples. (f) The TEM-EDS results of the NMO-C1T10 particles.

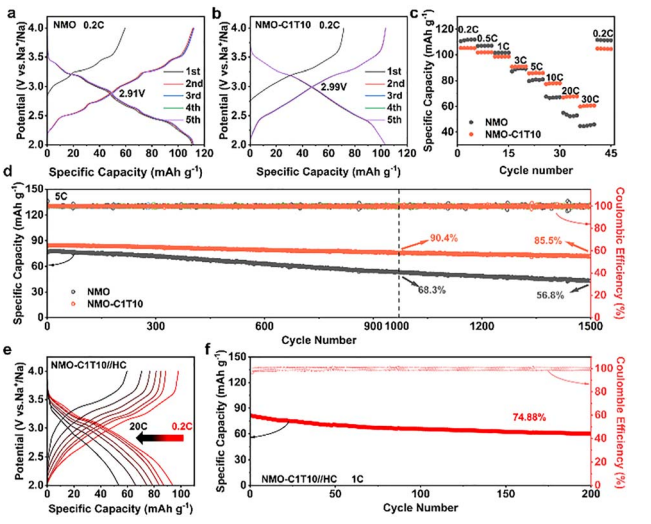

Fig. 2 The first five charge–discharge curves of (a) NMO and (b) NMO-C1T10 at 0.2C (1C = 120 mA g^{-1}). (c) Rate performances of the NMO and NMO-C1T10 cathodes. (d) Cycling performances of the NMO and NMO-C1T10 cathodes at 5C. (e) Galvanostatic charge/discharge profiles of the hard carbon//NMO-C1T10 full cell at different current densities. (f) Cycle performance and the corresponding coulombic efficiencies of the hard carbon//NMO-C1T10 full cell tested at 1C.

NMO-C1T10 was slightly lower than that of NMO, which results from the partial substitution of electrochemically active Mn sites by Ti^{4+}, the average operating voltage increased from 2.91 to 2.99 V. It is worth noting that the elevated output voltage and the solid–solution reaction behavior are primarily attributed to Ti doping (Fig. S9). By contrast, the Cu-doped sample (NMO-C1) inherited electrochemical features similar to those of the undoped NMO. In addition, Ti doping improves the initial charge/discharge efficiency (Fig. S10) and significantly enhances the electrochemical reaction reversibility by optimizing the lattice tunnel structure. Moreover, NMO-C1T10 delivered a discharge capacity of 105.3 mA h g^{-1} at 0.2C and retained 63.6% of this capacity at 30C (40.4% for the NMO cathode, Fig. 2c). This is mainly attributed to enhanced sodium-ion kinetics enabled by Cu doping (Fig. S11). Notably, NMO-C1 exhibits superior rate capability, which is attributed to the expanded intrinsic S-type Na^+ diffusion channels to optimize sodium ion transport channels. Long-term cycling stability was evaluated at a high current density of 600 mA g^{-1} (Fig. 2d and S12). NMO-C1T10 exhibits an improved capacity retention of 85.5% compared to those of NMO (56.8%), Ti-doped NMO (79.0%), and Cu-doped NMO (61.5%) after 1500 cycles at 5C. Compared with other reported materials, NMO-C1T10 delivers superior cycling performance (Fig. S13),[38–44] further demonstrating its great potential for high-power and long-cycle sodium-ion battery applications. To accurately assess the intrinsic structural stability of the electrodes with minimized polarization effects, additional cycling tests were conducted at a lower current density of 120 mA g^{-1}. The capacity retention in the 200th cycle for NMO and NMO-C1T10 was 86.5% and 95.9%, respectively (Fig. S14).

To evaluate practical applicability of the NMO-C1T10 cathode, a full cell was constructed with the NMO-C1T10 cathode and a pre-sodiated hard carbon anode within a voltage window of 2.0–4.0 V (Fig. S15). It delivers an initial discharge capacity of 93.72 mA h g^{-1} at 0.2C (Fig. 2e), retaining 56.9% of this capacity at 20C. Furthermore, the capacity retention reaches 74.88% after 200 cycles at 1C (Fig. 2f). The SEM and HRTEM images further confirm the structural stability of NMO-C1T10. As shown in Fig. S16 and S17, NMO-C1T10 retains its intact rod-like morphology and crystal integrity with clear continuous lattice fringes on the particle surface after long-term cycling. By contrast, NMO undergoes severe morphological degradation, including particle cracking and pulverization. Repeated Na^+ insertion/extraction triggers complex phase transitions in NMO, leading to surface structural deterioration and lattice amorphization. This irreversible structural damage results in rapid capacity decay and poor cycling stability.

In situ X-ray diffraction (XRD) was employed to explore the effect of Cu/Ti doping on the phase evolution throughout the charge–discharge process, as displayed in Fig. 3a, b, and S18. The (130), (140), (160), and (350) diffraction peaks shift systematically to higher 2θ angles during charging, corresponding to a uniform lattice contraction. This contraction is attributed to the increased electrostatic repulsion between oxygen atoms upon Na^+ removal. A distinct different evolution is observed in the peak of (350). NMO undergoes abrupt peak

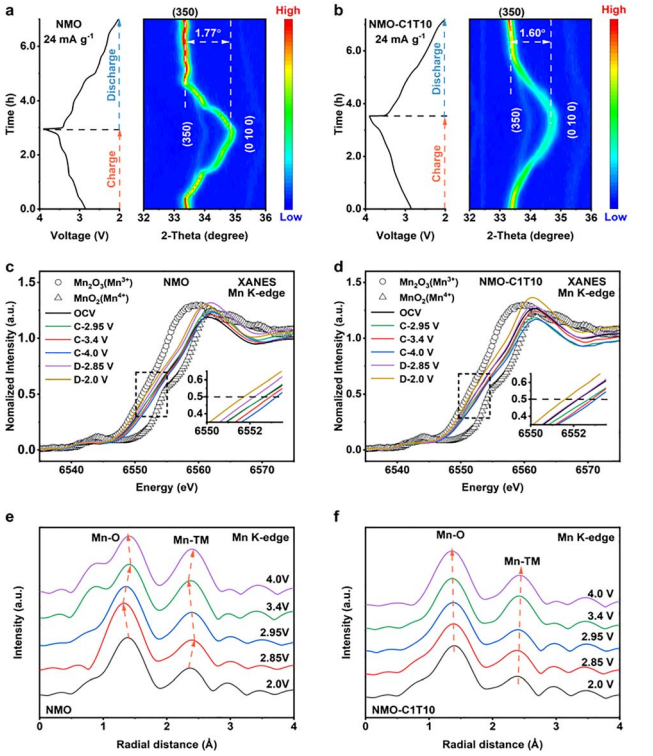

Fig. 3 *In situ* XRD of (a) NMO and (b) NMO-C1T10. The corresponding Mn K-edge XAS spectra of (c) NMO and (d) NMO-C1T10 at various charge/discharge states. *R*-Space XANES spectra of Mn K-edge of (e) NMO and (f) NMO-C1T10 at different charge/discharge states.

shifts between 3.0 and 4.0 V, reflecting multi-phase transitions, while NMO-C1T10 shows smooth, continuous shifts characteristic of a solid-solution reaction. Notably, the suppressed structural change in NMO-C1T10 is directly evidenced by the smaller angular shift of the (350) peak (1.60°) compared to that in NMO (1.77°). Furthermore, the refinement results (Fig. S19) show that the variations of *a*, *b* and *c* lattice parameters in NMO are 0.162 Å, 1.27 Å and 0.03 Å, respectively. Of note, the Cu/Ti co-doped NMO-C1T10 displays suppressed lattice strain, with the corresponding variations reduced to 0.118 Å, 1.09 Å, and 0.02 Å. The mitigated lattice contraction and expansion of NMO-C1T10 demonstrate that the synergistic effect of Cu and Ti doping effectively stabilizes the tunnel crystal framework.

The charge compensation mechanism in NMO and Cu/Ti-doped NMO-C1T10 was investigated by X-ray Absorption Spectroscopy (XAS). As shown in Fig. 3c and d, the Mn K-edge XANES spectra shift toward the higher energy from the OCV state to 4.0 V upon the initial Na^+ extraction from NMO and NMO-C1T10, demonstrating the oxidation of Mn^{3+} to Mn^{4+}. After the 1st discharge to 2.0 V, the shift of Mn K-edge XANES spectra toward lower energy indicates the reduction of Mn^{4+} to Mn^{3+} during discharge. The local structure was further investigated through *ex situ* Mn K-edge EXAFS spectroscopy (Fig. 3e and f). In the selected state of charge, the Mn–O bond length distribution of NMO fluctuates significantly, while that of NMO-C1T10 remains almost unchanged. The regularity of NMO's Mn–O bond length distribution is much poorer than that of NMO-

C1T10. This indicates that the Jahn–Teller effect of Mn induces obvious structural distortion in NMO during this process, leading to a sharp decrease in its Mn–O coordination order. In contrast, dual doping effectively suppresses the Jahn–Teller distortion of Mn in NMO-C1T10, improves the Mn–O coordination order and stabilizes the bond length distribution, thus ultimately enhancing the structural stability of the material.

X-ray Photoelectron Spectroscopy (XPS) was also conducted. The results confirm that manganese redox serves as the primary charge compensation mechanism in both materials (Fig. S20), while Cu^{2+} and Ti^{4+} dopants remain in their initial oxidation states without change during cycling (Fig. S21). In addition, XPS measurements provide quantitative evidence of oxidation state changes. The Mn 3s spectrum of NMO-C1T10 shows increased peak splitting (5.11 eV) compared to NMO (4.90 eV), indicating a lower average manganese oxidation state (Fig. S22). The Mn 2p XPS spectra also indicated that the Mn^{3+}/Mn^{4+} ratio in NMO-C1T10 increases to 0.95 (0.78 in NMO). These results arise from the substitution of Mn^{3+} with lower-valence Cu^{2+}.

To evaluate the electrochemical reaction kinetics, cyclic voltammetry (CV) measurements were performed on the as prepared samples at various scan rates (0.1 to 0.7 mV s^{-1}). The resulting CV curves are shown in Fig. 4a, b and S23. The linear relationships between the peak current (I_p) and the square root of the scan rate ($v^{1/2}$), as shown in Fig. 4c, demonstrate a diffusion-controlled process for the whole electrode reaction. The chemical diffusion coefficients (D) of Na^+ in NMO and NMO-C1T10 were then evaluated using the Randles–Sevcik equation (eqn (S1)).[45,46] D values of the anodic reactions in NMO and NMO-C1T10 are calculated to be 3.66×10^{-9} cm^2 s^{-1} and 5.59×10^{-9} cm^2 s^{-1}, respectively. Notably, the fitted lines in Fig. 4c do not pass through the origin as described in eqn (S1). This is because the calculated b-values of the NMO and NMO-C1T10 samples derived from the power-law equation (eqn (S2)) confirm the presence of pseudocapacitive behavior in both materials (Fig. S24). Moreover, the Na^+ diffusion coefficients of NMO-C1T10 obtained from galvanostatic intermittent titration technique (GITT) measurements are on the order of 10^{-11} to 10^{-10} cm^2 s^{-1}, which are significantly higher than those of the pristine NMO (Fig. S25).

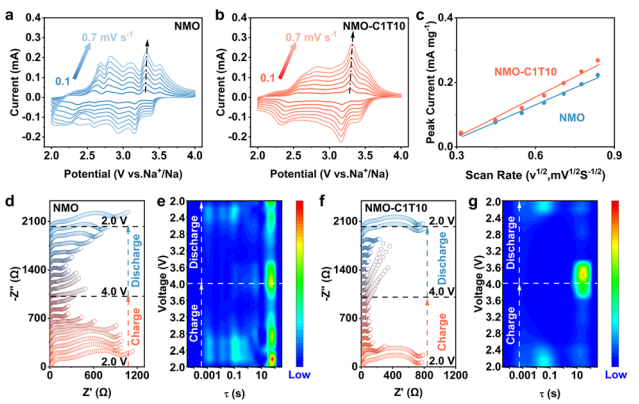

Fig. 4 CV curves of (a) NMO and (b) NMO-C1T10 cathodes at various scan rates (0.1, 0.2, 0.3, 0.4, 0.5, 0.6 and 0.7 mV s^{-1}). (c) Plots of peak current *versus* the square root of the scan rate for the NMO and NMO-C1T10 cathodes. *In situ* EIS of (d) NMO and (f) NMO-C1T10 during the second cycle. DRT analysis of (e) NMO and (g) NMO-C1T10.

In situ electrochemical impedance spectroscopy (EIS) spectra and the corresponding distribution of relaxation times analysis are shown in Fig. 4d–g. All Nyquist plots are composed of two semicircles in the high-to-medium frequency region and an inclined line in the low-frequency region. These features are assigned to the inter-particle contact resistance, the charge-transfer resistance (R_{ct}) at the electrolyte/electrode interface, and the Warburg impedance associated with Na^+ solid-state diffusion, respectively. The evolution indicates that the R_{ct} gradually decreases with the Na^+ extraction and presents an opposite trend during the Na^+ insertion process, correlating with a higher Na^+ content raising the migration barrier. Notably, NMO-C1T10 retains lower resistance throughout cycling, demonstrating its superior electrode kinetics. Furthermore, distribution of relaxation times (DRT) was used to isolate and resolve highly overlapping physicochemical processes in EIS. The *in situ* EIS of NMO and NMO-C1T10 in the second cycle were recorded (Fig. 4d and f) and analyzed by the DRT technique (Fig. 4e and g). Based on the time constants, frequency ranges and the actual Na^+ reaction processes, the DRT peaks were assigned to five physical models, including contact ohmic resistance (τ_1); Na^+ transport through the solid electrolyte interface (CEI) layer on the cathode surface (τ_2/τ_3); charge transfer interfacial resistance (τ_4, R_{ct}), and solid-state diffusion of Na^+ in the bulk (τ_5). For NMO-C1T10, the τ_5 peak exhibits altered bulk phase Na^+ transport characteristics arising from phase structural evolution, yet this variation exerts a negligible influence on the overall DRT peak profile. This phenomenon is attributed to the high R-value intrinsic to the pristine structure, which endows the material with rapid bulk Na^+ transport kinetics. In comparison with pristine NMO, NMO-C1T10 displays highly symmetric τ_4 and τ_5 peaks during both charging and discharging processes, which indicates the excellent reversibility of its structural phase transition.

Density functional theory (DFT) calculations were performed to elucidate the Na^+ diffusion mechanism and the corresponding electronic structure characteristics. To determine the most stable configuration, the total energies of five potential Cu doping sites were analyzed. The configuration with Cu occupying the Mn5 site has the lowest total energy (Fig. 5a). The optimized structures reveal distinct local effects of each dopant and the co-doping mechanism is summarized in Fig. 5b. Ti doping at the Mn3 site shortens Ti–O bonds in TiO6 octahedra compared to the original Mn(3)O6, reducing the local ligand volume and stabilize the structure during cycling (Fig. S26). In contrast, Cu^{2+} doping at the Mn5 site elongates Cu–O bonds in CuO5 square pyramids relative to Mn(5)O5 polyhedra (Fig. S27), due to the larger ionic radius of Cu^{2+} (0.72 Å *vs.* Mn^{3+}: 0.65 Å (Table S4)) and greater electronic repulsion in its 3 d^9 configuration. Moreover, Cu doping expands the ligand volume at the Mn5 site (red dashed area), effectively widening the adjacent large S-type sodium channels. The channel expansion facilitated rate capability of NMO-C1T10. The density of states (DOS) of NMO and NMO-C1T10 are illustrated in Fig. S28. The electronic states of Mn near the Fermi level are predominantly

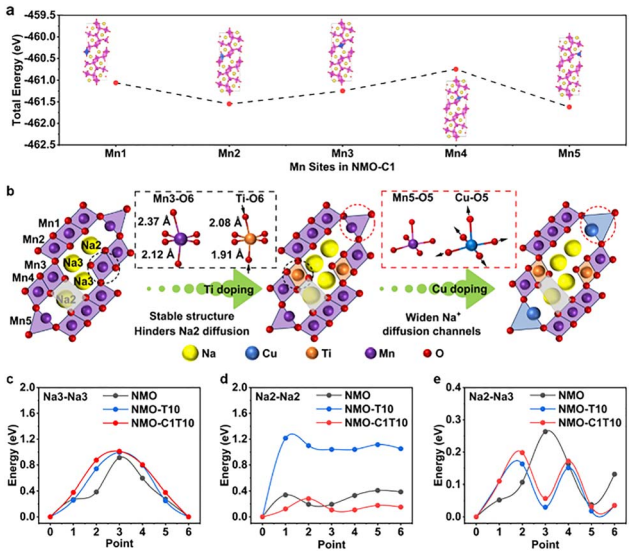

Fig. 5 (a) Total energies with the corresponding crystal structures of the NMO-C1 structure with five potential Cu-doped Mn5 sites. (b) Schematic illustration of the Cu/Ti Co-doping mechanism in NMO cathode materials. Sodium diffusion energy barriers for NMO, NMO-T10, and NMO-C1T10 in different migration pathways: (c) Na3–Na3, (d) Na2–Na2, and (e) Na2–Na3.

derived from Mn 3d orbitals. In NMO-C1T10, these states shift closer toward the Fermi energy compared to those in the undoped NMO, indicating enhanced redox activity in the co-doped cathode.

To investigate the impact of doping on Na^+ migration, the climbing-image nudged elastic band (CI-NEB) method was used to compute the migration barriers in NMO and NMO-C1T10. As illustrated in Fig. 5c–e, the three predominant diffusion pathways are axial diffusion of Na2 ions, axial diffusion of Na3 ions along the *Z*-axis, and the mutual exchange diffusion of Na2 and Na3 ions within the ab-plane, respectively. DFT calculations reveal that Cu/Ti co-doping effectively reduces the overall Na^+ diffusion barriers. While the Na3–Na3 barrier remains stable across materials, the critical Na2–Na2 barrier in NMO-C1T10 is restored to a low value comparable to that of pristine NMO, and the Na2–Na3 barrier is simultaneously lowered. This indicates that co-doping not only facilitates ion migration but also increases the proportion of direct Na2-site diffusion along the *Z*-axis, demonstrating a shift in pathway preference, which aligns with the more Na2 extraction in NMO-C1T10 observed by XRD refinement (Fig. S29–S32 and Tables S5–S8). The lowered energy barriers and optimized diffusion path distribution collectively contribute to the superior rate performance of NMO-C1T10.

Conclusions

In summary, we demonstrate that the rationally designed Cu/Ti co-doping strategy in tunnel-type $Na_{0.44}MnO_2$ significantly enhances both structural stability and Na^+ diffusion kinetics. The site-specific substitution of Cu^{2+} at the Mn5 site widens the Na^+ diffusion channels and enhances electronic conductivity, while Ti^{4+} acts as a structural pillar at the Mn3 site to suppress phase transitions and Jahn–Teller distortion. These synergetic effects lower the Na^+ diffusion energy barriers, optimize ion transport pathways, and ensure structural integrity during cycling. Consequently, the NMO-C1T10 cathode achieves exceptional performance, retaining 90.4% capacity after 1000 cycles at 600 mA g^{-1}. Beyond providing a high-performance material, this study establishes a general design principle for optimizing intercalation electrodes *via* atomic-scale control of crystallographic sites.

Author contributions

Z. H. and C. W. conceived and designed the experiments. C. X. conducted the experiments and prepared the supplementary materials. Z. H. performed DFT calculations. C. X. wrote the manuscript. All authors analyzed the data, discussed the results and approved the manuscript.

Conflicts of interest

There are no conflicts to declare.

Data availability

The data supporting this article have been included as part of the supplementary information (SI). Supplementary information: experimental details, spectroscopic data for the compounds, X-ray crystallographic details, and theoretical calculation details. See DOI: https://doi.org/10.1039/d6sc02363k.

Acknowledgements

This work was supported by the Ministry of Science and Technology of China (Grant Number: 2022YFB2402300); the National Natural Science Foundation of China (Grant Number: 22209116), the Shenzhen Science and Technology Program (KQTD20221101093605019), the Shenzhen Key Research Project (No. KCXFZ20240903094159005), and the fund of Department of Education of Guangdong Province for Higher Educational Institution (No. 2024KCXTD064). The authors appreciate the support from the Guangdong Provincial Key Laboratory of New Energy Materials Service Safety. The authors appreciate the Instrumental Analysis Center of Shenzhen University (Lihu Campus) and the Electron Microscopy Center of Shenzhen University for assistance with the materials characterization.

Notes and references

1 X. Yang, H. Zhang, Q. Liu and G. Jiang, *Nat. Rev. Chem.*, 2025, **9**, 497–498.
2 S. N. Lauro, J. N. Burrow and C. B. Mullins, *eScience*, 2023, **3**, 100152.
3 K. D. Jones, C. Zor, G. Rees, S. Yang, A. Pateman, X. Gao, P. G. Bruce and L. R. Johnson, *ECS Meet. Abstr.*, 2025, 516.
4 E. Gabriel, C. Ma, K. Graff, A. Conrado, D. Hou and H. Xiong, *eScience*, 2023, **3**, 100139.

5 N. Tapia-Ruiz, C. Soares, J. W. Somerville, R. A. House, J. Billaud, M. R. Roberts and P. G. Bruce, *J. Power Sources*, 2021, **506**, 230104.
6 S. Mariyappan, P. Desai, M. Morcrette and J.-M. Tarascon, *Nat Sustain*, 2025, **9**, 360–371.
7 Y. Niu, Y. Guo, Y. Yin, S. Zhang, T. Wang, P. Wang, S. Xin and Y. Guo, *Adv. Mater.*, 2020, **32**, 2001419.
8 C. Yang, H. Ma, R. Yuan, K. Wang, K. Liu, Y. Long, F. Xu, L. Li, H. Zhang, Y. Zhang, X. Li and H. Wu, *Nat. Energy*, 2023, **8**, 703–713.
9 S. Chen, G. Wu, H. Jiang, J. Wang, T. Chen, C. Han, W. Wang, R. Yang, J. Zhao, Z. Tang, X. Gong, C. Li, M. Zhu, K. Zhang, Y. Xu, Y. Wang, Z. Hu, P. Chen, B. Wang, K. Zhang, Y. Xia, H. Peng and Y. Gao, *Nature*, 2025, **638**, 676–683.
10 L. Hu, P. Hu, Q. Zhang, J. Cong, W. Su, Y. Ren, Y. Kong, J. Zhang, Z. Li and Y. Huang, *Energy Storage Mater.*, 2025, **81**, 104500.
11 X. Zhang, J. Chen, J. Ye, T. Zhang and Z. Hou, *Adv. Energy Mater.*, 2023, **13**, 2204413.
12 X. He, J. Wang, B. Qiu, E. Paillard, C. Ma, X. Cao, H. Liu, M. C. Stan, H. Liu, T. Gallash, Y. S. Meng and J. Li, *Nano Energy*, 2016, **27**, 602–610.
13 M. S. Chae, H. J. Kim, H. Bu, J. Lyoo, R. Attias, B. Dlugatch, M. Oliel, Y. Gofer, S. Hong and D. Aurbach, *Adv. Energy Mater.*, 2020, **10**, 2000564.
14 Q. Ding, W. Zheng, A. Zhao, Y. Zhao, K. Chen, X. Zhou, H. Zhang, Q. Li, X. Ai, H. Yang, Y. Fang and Y. Cao, *Adv. Energy Mater.*, 2023, **13**, 2203802.
15 X.-Y. Zhang, L.-Y. Kong, J. Ding, Y.-F. Zhu, J.-Y. Li, Z.-C. Jian, H. Xin, M.-Y. Li, P. Tan, W. K. Pang, S.-X. Dou and Y. Xiao, *ACS Energy Lett.*, 2025, **10**, 2858–2867.
16 X. Zhu, F. Meng, Q. Zhang, L. Xue, H. Zhu, S. Lan, Q. Liu, J. Zhao, Y. Zhuang, Q. Guo, B. Liu, L. Gu, X. Lu, Y. Ren and H. Xia, *Nat Sustain*, 2020, **4**, 392–401.
17 J. Lin, X. Chen, E. Fan, X. Zhang, R. Chen, F. Wu and L. Li, *eScience*, 2023, **3**, 100110.
18 Y. Zhang, A. Hu, D. Xia, S. Hwang, S. Sainio, D. Nordlund, F. M. Michel, R. B. Moore, L. Li and F. Lin, *Nat. Nanotechnol.*, 2023, **18**, 790–797.
19 F. Liedy, J. Eng, R. McNab, R. Inglis, T. J. Penfold, E. K. Brechin and J. O. Johansson, *Nat. Chem.*, 2020, **12**, 452–458.
20 W. J. Kim, M. A. Smeaton, C. Jia, B. H. Goodge, B.-G. Cho, K. Lee, M. Osada, D. Jost, A. V. Ievlev, B. Moritz, L. F. Kourkoutis, T. P. Devereaux and H. Y. Hwang, *Nature*, 2023, **615**, 237–243.
21 Y. Wang, J. Liu, B. Lee, R. Qiao, Z. Yang, S. Xu, X. Yu, L. Gu, Y.-S. Hu, W. Yang, K. Kang, H. Li, X.-Q. Yang, L. Chen and X. Huang, *Nat. Commun.*, 2015, **6**, 6401.
22 D. Wang, C. Shi, Y.-P. Deng, Z. Wu, Z. Yang, Y. Zhong, Y. Jiang, B. Zhong, L. Huang, X. Guo and Z. Chen, *Nano Energy*, 2020, **70**, 104539.
23 K. Wang, G. Guo, X. Tan, L. Zheng and H. Zhang, *Chem. Eng. J.*, 2023, **451**, 139059.
24 P. Ji, C. Zhang, J. Wan, M. Zhou, Y. Xi, H. Guo, C. Hu, X. Gu, C. Wang and W. Xue, *ACS Appl. Mater. Interfaces*, 2019, **11**, 28900–28908.
25 F. Dong, B. Yang, X. Zhang, Z. Yang, S. Wang, Z. Hou and P. Chen, *ACS Appl. Mater. Interfaces*, 2025, **17**, 1332–1340.
26 S. Xu, Y. Wang, L. Ben, Y. Lyu, N. Song, Z. Yang, Y. Li, L. Mu, H. Yang, L. Gu, Y. Hu, H. Li, Z. Cheng, L. Chen and X. Huang, *Adv. Energy Mater.*, 2015, **5**, 1501156.
27 Q.-C. Wang, Q.-Q. Qiu, N. Xiao, Z.-W. Fu, X.-J. Wu, X.-Q. Yang and Y.-N. Zhou, *Energy Storage Mater.*, 2018, **15**, 1–7.
28 X. Liang, H. Kim, H. Jung and Y. Sun, *Adv. Funct. Mater.*, 2021, **31**, 2008569.
29 W.-J. Shi, H.-X. Li, D. Zhang, F.-H. Du, Y.-H. Zhang, Z.-Y. Wang, X.-H. Zhang and P.-F. Zhang, *Chem. Eng. J.*, 2023, **477**, 146976.
30 X. Li, J. Bao, Y. Li, D. Chen, C. Ma, Q. Qiu, X. Yue, Q. Wang and Y. Zhou, *Adv. Sci.*, 2021, **8**, 2004448.
31 H. Zhang, Y. Xiang, B. Liu, G. Li, C. Dun, H. Huang, Q. Zou, L. Xiong and X. Wu, *J. Colloid Interface Sci.*, 2024, **661**, 389–400.
32 Z. M. Liu, X. T. Feng, H. J. Zhao, X. Q. Han, Z. X. Ye, Z. C. Yao and D. Zhang, *ACS Omega*, 2025, **10**, 10023–10033.
33 M. S. Chae, A. Chakraborty, S. Kunnikuruvan, R. Attias, S. Maddukuri, Y. Gofer, D. T. Major and D. Aurbach, *Adv. Energy Mater.*, 2020, **10**, 2002077.
34 H. Liu, L. Kong, H. Wang, J. Li, J. Wang, Y. Zhu, H. Li, Z. Jian, X. Jia, Y. Su, S. Zhang, J. Mao, S. Chen, Y. Liu, S. Chou and Y. Xiao, *Adv. Mater.*, 2024, **36**, 2407994.
35 H. Kim, D. J. Kim, D.-H. Seo, M. S. Yeom, K. Kang, D. K. Kim and Y. Jung, *Chem. Mater.*, 2012, **24**, 1205–1211.
36 F. Sauvage, L. Laffont, J.-M. Tarascon and E. Baudrin, *Inorg. Chem.*, 2007, **46**, 3289–3294.
37 X. Zhou, T. Liu, C. Cheng, X. Xia, Y. Shen, L. Wang, Y. Xie, B. Wang, Y. Zou, D. Cao, Y. Su and L. Zhang, *Energy Storage Mater.*, 2025, **74**, 103895.
38 H. Liu, R. Feng, F. Hussain, L. Wang, Q. Fan, M. Ni, C. Qiu, M. Sun, J. Wang, T. Wang, Z. Shi, X. Zhu and H. Xia, *Adv. Funct. Mater.*, 2024, **34**, 2404442.
39 Y. Xiao, Y. Zhu, W. Xiang, Z. Wu, Y. Li, J. Lai, S. Li, E. Wang, Z. Yang, C. Xu, B. Zhong and X. Guo, *Angew. Chem., Int. Ed.*, 2020, **59**, 1491–1495.
40 W.-J. Shi, Y.-W. Yan, C. Chi, X.-T. Ma, D. Zhang, S.-D. Xu, L. Chen, X.-M. Wang and S.-B. Liu, *J. Power Sources*, 2019, **427**, 129–137.
41 W.-J. Shi, D. Zhang, X.-M. Meng, C.-X. Bao, S.-D. Xu, L. Chen, X.-M. Wang, S.-B. Liu and Y.-C. Wu, *ACS Appl. Mater. Interfaces*, 2020, **12**, 14174–14184.
42 W. Shi, Y. Zheng, X. Meng, S. Liu, S. Xu, L. Chen, X. Wang and D. Zhang, *ChemElectroChem*, 2020, **7**, 2545–2552.
43 H. Gong, Y. Zhang, Z. Jiao, W. Mao and L. Wang, *Electrochim. Acta*, 2025, **527**, 146156.
44 W. Ni, Q. Ding, W. Zheng, G. Peng, H. Wang, Z. Xie and Y. Cao, *ACS Appl. Mater. Interfaces*, 2024, **16**, 64725–64735.
45 K. Tang, X. Yu, J. Sun, H. Li and X. Huang, *Electrochim. Acta*, 2011, **56**, 4869–4875.
46 J.-L. Yue, Y.-N. Zhou, X. Yu, S.-M. Bak, X.-Q. Yang and Z.-W. Fu, *J. Mater. Chem. A*, 2015, **3**, 23261–23267.